

Dipole response of deformed halo nuclei ^{31}Ne and ^{37}Mg

Xiao Lu,^{1,*} Hiroyuki Sagawa,^{1,2,3,†} and Shan-Gui Zhou^{1,4,5,‡}

¹*CAS Key Laboratory of Theoretical Physics, Institute of Theoretical Physics,
Chinese Academy of Sciences, Beijing 100190, China*

²*RIKEN Nishina Center for Accelerator-Based Science, Wako 351-0198, Japan*

³*Center for Mathematics and Physics University of Aizu, Aizu Wakamatsu, Fukushima 965-0001, Japan*

⁴*School of Physical Sciences, University of Chinese Academy of Sciences, Beijing 100049, China*

⁵*School of Nuclear Science and Technology, University of Chinese Academy of Sciences, Beijing 100049, China*

(Dated: December 31, 2024)

We study the soft electric dipole ($E1$) response of deformed halo nuclei ^{31}Ne and ^{37}Mg using a deformed Woods-Saxon potential, with the potential depth adjusted to reproduce empirical separation energy of last neutron orbit, i.e., 150 keV for ^{31}Ne and 220 keV for ^{37}Mg . The configuration dependence of the $E1$ strength near the neutron threshold is pointed out. The halo configurations $[321]3/2$ at $\beta_2 = 0.5$ and $[330]1/2$ at $\beta_2 = 0.24$ in ^{31}Ne contain large amplitudes of halo p -shell orbits, which significantly enhance the threshold strength by several times compared to the non-halo configuration $[202]5/2$ at $\beta_2 = 0.32$. In ^{37}Mg , the last neutron configuration is assigned as $[321]1/2$ at a large deformation of $\beta_2 = 0.46$, which involves a halo p -shell configuration that significantly enhances the soft dipole strength. This enhancement is about 60% larger than that of the $[321]3/2$ configuration in ^{31}Ne because of large p -shell probability in ^{37}Mg . Experimental confirmation of the soft dipole strength is highly desired to determine the deformation and the configuration of the last neutron orbits both in ^{31}Ne and ^{37}Mg .

I. INTRODUCTION

Structural evolution of atomic nuclei towards the neutron and proton drip lines in the nuclear chart is one of the most important and intriguing issues in current nuclear physics. In particular, the location of the neutron drip line is the key to understanding the stability of the nuclear many-body quantum system. Nuclei exhibit a peculiar feature of nuclear structure, such as the neutron halo nuclei found in the vicinity of the neutron drip line [1–3]. A halo structure appears as an extended density distribution, which is one of the characteristic features of weakly bound neutron-rich and proton-rich nuclei. It was first observed in ^{11}Li , which exhibits an abnormally large interaction cross section [4]. Other examples include ^{11}Be [5, 6] and ^{19}C [7, 8], both of which are typical one-neutron ($1n$) halo nuclei. Recently, the $1n$ halo nuclei ^{31}Ne [9, 10] and ^{37}Mg [11, 12], as well as the $2n$ halo nuclei ^{17}B [13, 14], ^{19}B [15], ^{22}C [16], and ^{29}F [17] have been identified. A key question is how these heavier halo nuclei can be formed and in which regions of the nuclear chart they occur, particularly when discussing nuclear structure near the drip line.

The halo is formed under the condition that the nucleus has a very small $1n$ or $2n$ separation energy ($S_n, S_{2n} \leq 1$ MeV) and that the least bound neutron has low angular momentum $l \leq 1$ [1, 18–22]. The latter condition is not satisfied for nuclei with $20 < N < 28$ when adopting the conventional single-particle shell model. This is because the least bound neutron in the $1f_{7/2}$ orbit

is affected by a large centrifugal barrier, which prevents the appearance of halo characteristics. As pointed out in Refs. [23, 24], open-shell nuclei with neutrons in the nearly degenerate $1f_{7/2}$ and $2p_{3/2}$ shells can induce a large quadrupole deformation in the ground state due to a strong quadrupole-quadrupole interaction among nucleons in these two orbits. This may also serve as a driving mechanism for the island of inversion, where many-particle many-hole configurations are dominant in the ground state. The one-particle motion in a deformed potential, such as the Nilsson diagram provides key insights into understanding the microscopic structure of such nuclei.

The halo structure induces a large concentration of electric dipole ($E1$) strength in the low-excitation energy region, which is referred to as soft dipole excitation [8, 25, 26]. Recently, the Coulomb breakup cross sections for ^{31}Ne were measured by Nakamura et al. [9, 10], indicating a soft dipole excitation in the ^{31}Ne nucleus. Notice that a naive spherical shell model leads to the $1f_{7/2}$ configuration for the valence neutron of ^{31}Ne . In order to generate the halo structure within the mean-field framework, the valence neutron therefore needs to move in a deformed mean-field potential, where the s or p wave component of a weakly-bound single-particle wave function makes a dominant contribution [27, 28].

Theoretically, deformed halo nuclei have been studied within the Nilsson model [24, 28, 29], the particle-rotor model [30–32], the shell model [33, 34], the cluster model [35], the deformed relativistic Hartree-Bogoliubov theory in continuum (DRHBc) [36–49], and anti-symmetrized molecular dynamics (AMD) model [50]. In this paper, we adopt a deformed Woods-Saxon model to study the intrinsic deformation effects on the dipole response of these nuclei. For largely deformed nuclei, the adiabatic

* luxiao@itp.ac.cn

† hiroyuki.sagawa@gmail.com

‡ sgzhou@itp.ac.cn

approach, such as the Nilsson model and the deformed Woods-Saxon model, is adequate to examine the general features of deformation in the excitation spectrum and the transition rate. Additionally, we can easily implement the halo nature of loosely bound nucleons in the low-energy response by constraining the empirical separation energy in the deformed wave function.

The main aim of this paper is to study how deformed halo affects the soft dipole excitation near the neutron threshold. Specifically, we will investigate the configuration dependence and the separation energy dependence of dipole response using the deformed Woods-Saxon potential. As examples, we select typical deformed halo nuclei with mass greater than $A = 20$, ^{31}Ne and ^{37}Mg . This paper is organized as follows: Section II is devoted to the basic formalism. The results are presented in Section III. The summary and future perspectives are given in Section IV.

II. THEORETICAL FRAMEWORK

We begin with our formulation of halo wave function for a spherical shape. The neutron bound-state wave function is obtained as an eigenfunction of the Woods-Saxon potential with an energy eigenvalue $\varepsilon < 0$

$$\left| \Phi^{(b)} : \ell j m \right\rangle = \frac{1}{r} R_{n\ell j}^{(b)}(r) [Y_\ell \otimes \chi_{1/2}]_{jm}, \quad (1)$$

where the radial wave function $R_{n\ell j}^{(b)}(r)$ is a solution of Schrödinger equation in the coordinate space, and the normalization is given by

$$\int_0^\infty dr \left| R_{n\ell j}^{(b)}(r) \right|^2 = 1. \quad (2)$$

The single-neutron wave function in the continuum can be expressed in a plane wave approximation (PWA) for a real energy variable $\varepsilon > 0$ as

$$\begin{aligned} \left| \Phi_\varepsilon^{(c)} : \ell j m \right\rangle &= \frac{1}{r} R_{\ell j}^{(c)}(\varepsilon, r) [Y_\ell \otimes \chi_{1/2}]_{jm} \\ &= \sqrt{\frac{2\mu}{\hbar^2 \pi k}} [\cos(\delta_{\ell j}) k j_\ell(kr) - \sin(\delta_{\ell j}) k n_\ell(kr)] \\ &\quad \times [Y_\ell \otimes \chi_{1/2}]_{jm}, \end{aligned} \quad (3)$$

where $j_\ell(kr)$ and $n_\ell(kr)$ are the spherical Bessel functions of the first kind and the second kind, respectively, and

$$k^2 = \frac{2\mu\varepsilon}{\hbar^2}, \quad (4)$$

with the reduced mass $\mu = (A - 1)M/A$ for the system with the mass A . The phase shift is denoted as $\delta_{\ell j}$. The normalization of the radial wave function is expressed as

$$\int_0^\infty dr R_{\ell j}^{(c)*}(\varepsilon, r) R_{\ell j}^{(c)}(\varepsilon', r) = \delta(\varepsilon - \varepsilon'). \quad (5)$$

We consider the Hamiltonian for the deformed system,

$$H = -\frac{\hbar^2}{2\mu} \nabla^2 + V(\mathbf{r}), \quad (6)$$

where $V(\mathbf{r})$ is the single-particle potential for the valence neutron interacting with the deformed core, and \mathbf{r} is the coordinate of the valence neutron in the intrinsic frame. We use an axially symmetric deformed Woods-Saxon potential for V and expand it up to the linear order of the quadrupole deformation parameter β_2 as

$$\begin{aligned} V(\mathbf{r}) &= -V_{\text{WS}} \left(1 - F_{ls} r_0^2 (\mathbf{l} \cdot \mathbf{s}) \frac{1}{r} \frac{d}{dr} \right) f(r) \\ &\quad + V_{\text{WS}} R_0 \beta_2 \frac{df(r)}{dr} Y_{20}(\hat{\mathbf{r}}) \\ &\equiv V_0(r) + V_{\text{def}}(\mathbf{r}), \end{aligned} \quad (7)$$

where V_0 represents a spherical Woods-Saxon potential together with the spin-orbit (ls) force and V_{def} is the deformed part of the potential. $f(r)$ is given by

$$f(r) = \frac{1}{1 + \exp\left(\frac{r-R}{a}\right)}. \quad (8)$$

The values of the parameters in the potential except the depth V_{WS} are taken from Ref. [23]. For example, the diffuseness $a = 0.67$ fm and the radius $R = r_0 A^{1/3}$ with $r_0 = 1.27$ fm. The single-particle wave function in the deformed Woods-Saxon potential is obtained as

$$H|\phi_\Omega\rangle = \varepsilon_\Omega |\phi_\Omega\rangle, \quad (9)$$

where Ω represents the projection of single-particle angular-momentum along the symmetry axis, which is a good quantum number in the axially symmetric potential.

The electric dipole transition $I_i^\pi, K_i^\pi \rightarrow I_f^\pi, K_f^\pi$ is expressed in the laboratory frame as [23]

$$\begin{aligned} B(E1(\varepsilon); I_i^\pi, K_i^\pi \rightarrow I_f^\pi, K_f^\pi) &= (e_{\text{eff}}^n(E1))^2 \{ \langle I_i K_i 1 K_f - K_i | I_f K_f \rangle \\ &\quad \times \langle K_f^\pi(\varepsilon) | r Y_{1\nu=K_f-K_i} | K_i^\pi \rangle \\ &\quad + (-1)^{I_i+K_i} \langle I_i - K_i 1 K_f + K_i | I_f K_f \rangle \\ &\quad \times \langle K_f^\pi(\varepsilon) | r Y_{1\nu=K_i+K_f} | \widetilde{K_i^\pi} \rangle \}^2. \end{aligned} \quad (10)$$

For a single-nucleon halo nucleus, the initial states can be expressed by a single-particle state $|\phi_\Omega\rangle$ in Eq. (9) with $K_i = \Omega$, and the final state is given by the continuum wave function (3) assigning $I_f = j$ and $K_f = m$. The effective electric charge of neutrons from the center-of-mass frame is given by

$$e_{\text{eff}}^n(E1) = \frac{N_c Z_v - Z_c N_v}{A}, \quad (11)$$

where $N_c(N_v)$ and $Z_c(Z_v)$ are neutron and proton numbers of the core (valence) particles, respectively. For the

dipole transition, the second term in Eq. (10) contributes only for $K_i = 1/2$ state. However, it was shown that the contribution of the second term in Eq. (10) is very small for $[330]1/2$ configuration because of cancellation between major components [51]. Therefore it is neglected in our calculation. The dipole transition strength at the excitation energy ω in the continuum is then express as

$$\frac{dB(E1)}{d\omega} = \int d\varepsilon \delta(\omega - (\varepsilon + S)) \times B(E1(\varepsilon); I_i^\pi, K_i^\pi \rightarrow I_f^\pi, K_f^\pi), \quad (12)$$

where $S > 0$ is the separation energy of the last occupied neutron in the deformed Wood-Saxon potential and ε is the energy of continuum state in Eq. (3). The radial wave function in the initial wave function is expanded using spherical radial wave functions

$$R_{lj}(\varepsilon, r) = \sum_n c_{nlj} R_{nlj}(r). \quad (13)$$

In the present calculations, the spherical single-particle energy was truncated at 10 MeV, the orbital angular momentum was truncated at $l = 10$. In Ref. [29], only the halo components, s and p waves, of the deformed wave functions are considered in the dipole matrix elements. However, in the present study, all multipoles with $l \leq 4$ are taken into account in the dipole response calculations.

We should notice that, in the following discussion, we will use the asymptotic quantum-numbers $[Nn_z\Lambda]\Omega$ to denote the initial state. In the Nilsson orbit, N , n_z , Λ and Ω represent the total oscillator quantum number, the oscillator quantum number in the z -direction, the orbital angular momentum projected on the symmetry axis, and the projection of total angular momentum on the symmetry axis, respectively. For example, $\langle K_f^\pi | r Y_{1\nu=K_f-K_i} | K_i^\pi \rangle$ matrix element can be expressed as $\langle K_f^\pi | r Y_{1\nu=K_f-K_i} | [N_i n_{zi} \Lambda_i] \Omega_i = K_i^\pi \rangle$.

III. RESULTS AND DISCUSSIONS

A. Electric dipole response in ^{31}Ne

The measured low-excitation energies of the first 2^+ states of both ^{30}Ne [52] and ^{32}Ne [53] are consistent with the picture that these Ne isotopes lie inside the island of inversion. Moreover, the large Coulomb breakup cross section reported in Refs. [9, 10], which clearly indicates the halo nature of the ground state of ^{31}Ne , suggests a substantial contribution from the p component of the 21st neutron in the deformed mean field. It is also noted that the measured spin and magnetic moment of the ground state of ^{33}Mg , which has the same neutron number $N = 21$ as ^{31}Ne , are reported to be consistent with the interpretation of $I^\pi = \frac{3}{2}^-$ in Ref. [54].

Low-lying states of odd- A medium-heavy deformed nuclei are well approximated by one (quasi)particle moving

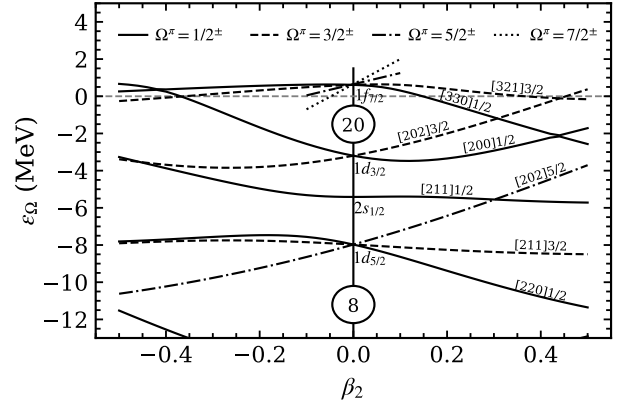


FIG. 1. Single-particle levels for neutrons in deformed Woods-Saxon potentials as a function of the quadrupole deformation parameter β_2 . The potential depth V_{WS} is adjusted so that the binding energy of the 21st neutron of the prolate deformed nucleus ^{31}Ne is 150 keV. The asymptotic quantum-numbers $[Nn_z\Lambda]\Omega$ are denoted for the single particle levels.

in the deformed potential produced by the even-even core [23]. The single-particle picture works better in deformed nuclei than in spherical nuclei, because the major part of the long-range residual interaction can be included in the deformed mean field, and consequently in the deformed wave function. The halo nature will be implemented in these wave functions by solving the Schrödinger equation in the coordinate space. The harmonic oscillator wave functions are often used in the standard shell model calculations, but their applicability to the description of halo nuclei is questionable [55].

Figure 1 shows the Nilsson diagram calculated by using deformed Woods-Saxon potential, whose parameters are adjusted for the separation energy of $S_n \sim 150$ keV of $(^{30}\text{Ne} + n)$ system. The one neutron outside the $N = 20$ core occupies the negative parity $[330]1/2$ orbit in the small deformation region $0.15 < \beta_2 < 0.3$, while it occupies $[321]3/2$ orbit at very large deformation $\beta_2 > 0.4$. In the medium deformation range, around $0.3 < \beta_2 < 0.4$, the last neutron occupies a positive parity $[202]3/2$ orbit. As shown in Tables I, II and III, $p_{3/2}$, $f_{5/2}$ and $f_{7/2}$ are included in the calculation of the $[321]3/2$, while the $p_{1/2}$, $p_{3/2}$, $f_{5/2}$ and $f_{7/2}$ are included in the calculation of the $[330]1/2$. In the calculation of the $[202]3/2$, the $d_{3/2}$ and $d_{5/2}$ orbits are included. It should be noted that the negative parity orbits in Tables I and II have significant contributions from the halo p -components in the deformed wave function, while the positive parity states in Table III have no halo component. The probability of $p_{3/2}$ component in $[321]3/2$ configuration is 32.7% which is almost identical to the value of 32% obtained by the Coulomb breakup cross section experiment in Ref. [10].

Due to the selection rules of the transition operator for calculating the $E1$ response, the final states can be s -wave, d -wave and g -wave. The configuration $[321]3/2$ is taken as the initial state with $I_i^\pi = K_i^\pi = \frac{3}{2}^-$, and the

TABLE I. The decomposition of the matrix elements $\langle K_f^\pi = \frac{3}{2}^+ | rY_{10} | [321] \rangle$, $\langle K_f^\pi = \frac{1}{2}^+ | rY_{1-1} | [321]3/2 \rangle$ and $\langle K_f^\pi = \frac{5}{2}^+ | rY_{11} | [321]3/2 \rangle$ in ^{31}Ne by contributions of spherical wave functions at the peak energy of the response $\varepsilon_{\text{peak}}$. The unit is fm.

Initial state	([321]3/2, $I_i^\pi = \frac{3}{2}^-$, $K_i^\pi = \frac{3}{2}^-$)			
Spherical configuration	$p_{3/2}$	$f_{5/2}$	$f_{7/2}$	
Probability	0.327	0.022	0.650	
$I_f^\pi = \frac{1}{2}^+, \frac{3}{2}^+, \frac{5}{2}^+$	$s_{1/2}$	-2.160		
	$d_{3/2}$	-0.070	-0.002	
$K_f^\pi = \frac{1}{2}^+$	$d_{5/2}$	0.085	-0.001	-0.040
	$g_{7/2}$		0.000	0.000
$\varepsilon_{\text{peak}} = 0.07 \text{ MeV}$	$g_{9/2}$			0.001
$I_f^\pi = \frac{3}{2}^+, \frac{5}{2}^+$	$d_{3/2}$	-0.339	-0.050	
	$d_{5/2}$	0.678	0.011	0.200
$K_f^\pi = \frac{3}{2}^+$	$g_{7/2}$		0.000	-0.006
	$g_{9/2}$			0.059
$\varepsilon_{\text{peak}} = 0.57 \text{ MeV}$				
$I_f^\pi = \frac{5}{2}^+, K_f^\pi = \frac{5}{2}^+$	$d_{5/2}$	1.087	-0.010	-0.061
	$g_{7/2}$		0.004	0.008
$\varepsilon_{\text{peak}} = 0.50 \text{ MeV}$	$g_{9/2}$			0.055

TABLE II. The decomposition of the matrix elements $\langle K_f^\pi = \frac{1}{2}^+ | rY_{10} | [330]1/2 \rangle$ and $\langle K_f^\pi = \frac{3}{2}^+ | rY_{11} | [330]1/2 \rangle$ in ^{31}Ne by contributions of spherical wave functions at the peak energy of the response $\varepsilon_{\text{peak}}$. The unit is fm.

Initial state	([330]1/2, $I_i^\pi = \frac{3}{2}^-$, $K_i^\pi = \frac{1}{2}^-$)			
Spherical configuration	$p_{1/2}$	$p_{3/2}$	$f_{5/2}$	$f_{7/2}$
Probability	0.063	0.590	0.004	0.342
$I_f^\pi = \frac{1}{2}^+, \frac{3}{2}^+, \frac{5}{2}^+$	$s_{1/2}$	-0.640	-2.650	
	$d_{3/2}$	0.136	0.057	-0.001
$K_f^\pi = \frac{1}{2}^+$	$d_{5/2}$		-0.421	0.000
	$g_{7/2}$			-0.001
$\varepsilon_{\text{peak}} = 0.09 \text{ MeV}$	$g_{9/2}$			-0.001
$I_f^\pi = \frac{3}{2}^+, \frac{5}{2}^+$	$d_{3/2}$	0.514	-0.423	-0.010
	$d_{5/2}$		-1.270	0.006
$K_f^\pi = \frac{3}{2}^+$	$g_{7/2}$		-0.002	-0.005
	$g_{9/2}$			-0.026

corresponding I_f^π and K_f^π are shown in Table I. Using Eqs. (10)-(12), we calculate the dipole strength distribution from the [321]3/2 configuration to six different final states, as well as the total strength distribution. The results are shown in Fig. 2, where the final angular momenta I_f^π are summed up for each K_f^π . It can be seen

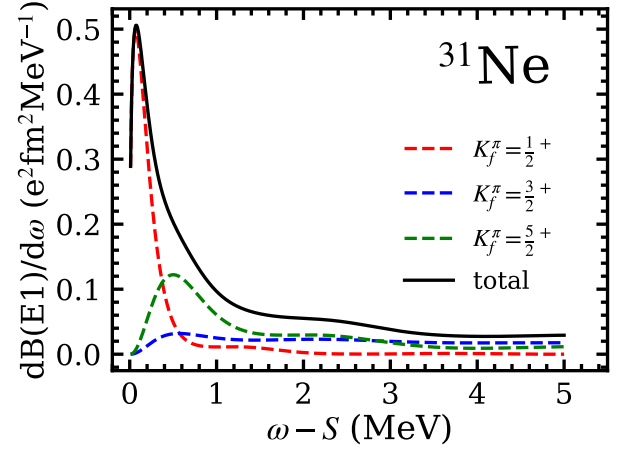


FIG. 2. (Color online) Dipole strength distribution calculated in PWA as function of the excitation energy (referred to the particle threshold). The wave function of the ground state takes the [321]3/2, $I_i^\pi = \frac{3}{2}^-$ configuration at $\beta_2 = 0.5$, which is calculated using the deformed Woods-Saxon potential, corresponding the single-neutron separation energy of 0.15 MeV. The $p_{3/2}$, $f_{5/2}$ and $f_{7/2}$ orbitals are included in the calculation of the [321]3/2 orbit. All final angular momenta I_f^π are summed up for each K_f^π in the figure.

that the $E1$ response to the $K_f^\pi = \frac{1}{2}^+$ state shows a very sharp peak just above the threshold, while the $K_f^\pi = \frac{3}{2}^+$ and $\frac{5}{2}^+$ states show relatively broad peaks at location slightly higher than the threshold. The contributions of these six states lead to an enhanced single-peak structure in the $E1$ strength distribution near the threshold.

The integrated strengths up to $\omega - S = 5 \text{ MeV}$ are listed in Table II. The total transition strength is much larger than the low-energy $E1$ transition in non-halo nuclei, which range from $10^{-3} \sim 10^{-4} \text{ e}^2\text{fm}^2$, but is smaller than the pure single-particle transition from a halo p -wave state having the same separation energy $S_n = 0.15 \text{ MeV}$ as the [321]3/2 configuration, as shown in Fig. 3. Since the responses to the configurations of $K_f^\pi = \frac{3}{2}^+$ and $K_f^\pi = \frac{5}{2}^+$ have no s -wave component of wave functions in the final states, they contribute to the dipole response with slightly higher energy and larger width than the sharp peak of $K_f^\pi = \frac{1}{2}^+$ configuration at $\varepsilon \sim 0.07 \text{ MeV}$ above the threshold. From Table I, it can be seen that this is due to 32.7% contribution from the $p_{3/2}$ component, along with a portion of the matrix elements from f -wave scattering to d - and g -waves that partially cancel the contribution to $E1$ response.

The $E1$ response from the initial state [330]1/2 at $\beta_2 = 0.24$ is shown in Fig. 4. For this configuration, the final states are limited to the states with $K_f^\pi = \frac{1}{2}^+$ and $\frac{3}{2}^+$. Again, the transitions to $K_f^\pi = \frac{1}{2}^+$ exhibit a sharp peak just above the threshold, while the $E1$ response to $K_f^\pi = \frac{3}{2}^+$ states shows a relatively broad peak at a location slightly higher than the threshold. We should note

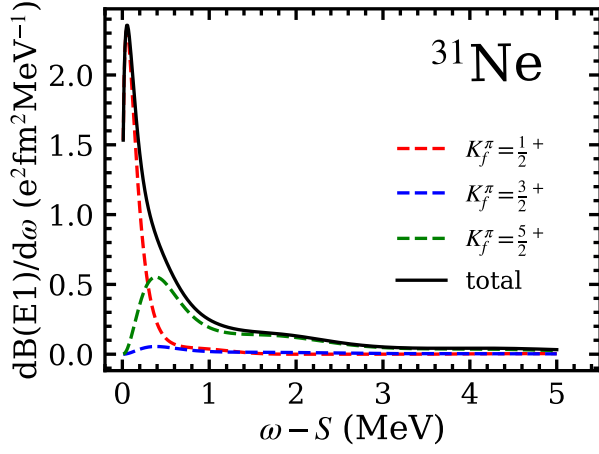


FIG. 3. (Color online) Same as Fig. 2, but for a pure single-particle halo $2p_{3/2}$ state taken from $[321]3/2$ configuration with the separation energy $S = 0.15$ MeV.

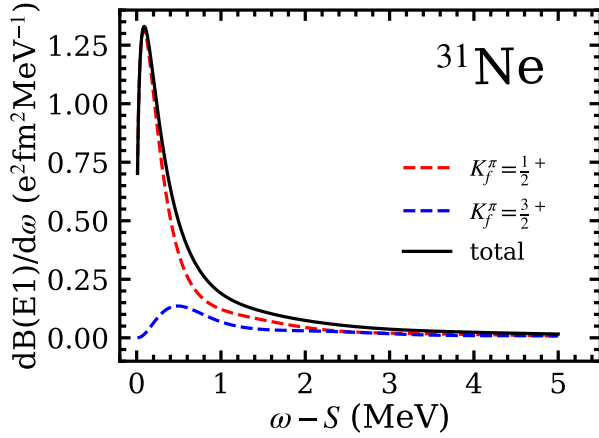


FIG. 4. (Color online) Same as Fig. 2, but for the wave function of the ground state $[330]1/2, I_i^\pi = \frac{3}{2}^-$ at $\beta_2 = 0.24$. The $p_{1/2}$, $p_{3/2}$, $f_{5/2}$ and $f_{7/2}$ orbitals are included in the calculation of the $[330]1/2$ orbit.

that the total $E1$ strength of the $[330]1/2$ configuration is nearly 2 times that of the $[321]3/2$ state, as shown in Table IV. This is because the halo p -wave component in the $[330]1/2$ state in Table II is almost twice as large as that in the $[321]3/2$ state.

The $E1$ response from $[202]3/2$ state is shown in Fig. 5. This positive parity configuration appears to be a possible $N = 21$ configuration in the medium deformation range at $\beta_2 \sim 0.3$. The dipole response shows a broad peak above the threshold, as there is no component of the halo s -wave in this Nilsson orbit, as tabulated in Table III. The integrated $E1$ strength, tabulated in Table IV, is also relatively smaller than those for the configurations $[330]1/2$ and $[321]3/2$. From the dipole response discussed here, it could be possible to distinguish the configuration of the last neutron in ^{31}Ne by looking at the enhancement of peak height, the width of peak and the

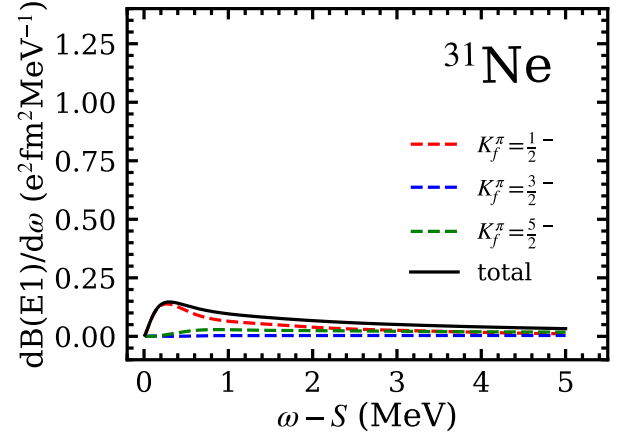


FIG. 5. (Color online) Same as Fig. 2, but for the different wave function of the ground state $[202]3/2, I_i^\pi = \frac{3}{2}^+$ at $\beta_{20} = 0.32$. The $d_{3/2}$ and $d_{5/2}$ orbitals are included in the calculation of the $[202]3/2$ orbit.

integrated dipole strength distribution as shown in Table IV.

TABLE III. The decomposition of the matrix elements $\langle K_f^\pi = \frac{3}{2}^- | rY_{10} | [202]3/2 \rangle$, $\langle K_f^\pi = \frac{1}{2}^- | rY_{1-1} | [202]3/2 \rangle$ and $\langle K_f^\pi = \frac{5}{2}^- | rY_{11} | [202]3/2 \rangle$ in ^{31}Ne by contributions of spherical wave functions at the peak energy of the response $\varepsilon_{\text{peak}}$. The unit is fm.

Initial state		($[202]3/2, I_i^\pi = \frac{3}{2}^+, K_i^\pi = \frac{3}{2}^+$)	
Spherical configuration		$d_{3/2}$	$d_{5/2}$
Probability		0.965	0.034
$I_f^\pi = \frac{1}{2}^-, \frac{3}{2}^-, \frac{5}{2}^-$	$p_{1/2}$	-0.865	
	$p_{3/2}$	-0.245	-0.124
	$f_{5/2}$	0.071	-0.007
$\varepsilon_{\text{peak}} = 0.27$ MeV		$f_{7/2}$	0.015
$I_f^\pi = \frac{3}{2}^-, \frac{5}{2}^-$	$p_{3/2}$	-0.115	0.041
	$f_{5/2}$	0.230	-0.008
	$f_{7/2}$		0.044
$\varepsilon_{\text{peak}} = 4.6$ MeV			
$I_f^\pi = \frac{5}{2}^-, K_f^\pi = \frac{5}{2}^-$	$f_{5/2}$	0.450	0.011
	$f_{7/2}$		0.067
$\varepsilon_{\text{peak}} = 0.87$ MeV			

In Ref. [29], the large Coulomb dissociation cross sections of ^{31}Ne was discussed by using a deformed Woods-Saxon potential with three possible configurations of $[Nn_z\Lambda]\Omega = [330]1/2$, $[321]3/2$, or $[200]1/2$. We note that the ground state with $I^\pi = \frac{3}{2}^-$ is predicted in the shell model calculations [56], as well as in the microscopic cluster model calculations [35] and in AMD calculations [50]. A decisive experimental information could be obtained from the soft dipole excitation near the neutron threshold.

TABLE IV. Dipole transition probabilities $B(E1)$ ($e^2\text{fm}^2$) for ^{31}Ne with different initial wave functions.

Initial state	[321]3/2 ($I_i^\pi = K_i^\pi = \frac{3}{2}^-$)	[330]1/2 ($I_i^\pi = \frac{3}{2}^-, K_i^\pi = \frac{1}{2}^-$)	[202]3/2 ($I_i^\pi = K_i^\pi = \frac{3}{2}^+$)	pure $2p_{3/2}$ ($I_i^\pi = K_i^\pi = \frac{3}{2}^-$)
$K_f^\pi = \frac{1}{2}^+$	0.147	0.655	0.212	0.519
$K_f^\pi = \frac{3}{2}^+$	0.103	0.176	0.016	0.064
$K_f^\pi = \frac{5}{2}^+$	0.164	—	0.106	0.638
Total	0.414	0.831	0.334	1.221

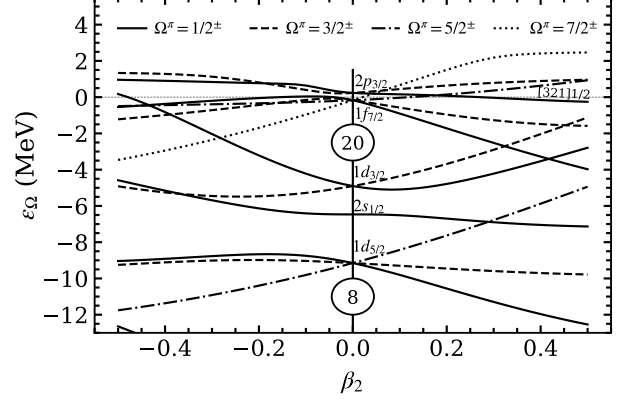
TABLE V. The decomposition of the matrix elements $\langle K_f^\pi = \frac{1}{2}^+ | rY_{10} | [321]1/2 \rangle$ and $\langle K_f^\pi = \frac{3}{2}^+ | rY_{11} | [321]1/2 \rangle$ in ^{37}Mg by contributions of spherical wave functions at the peak energy of the response $\varepsilon_{\text{peak}}$. The unit is fm.

Initial configuration	[321]1/2 ($I_i^\pi = \frac{3}{2}^-, K_i^\pi = \frac{1}{2}^-$)			
Spherical configuration	$p_{1/2}$	$p_{3/2}$	$f_{5/2}$	$f_{7/2}$
Probability	0.428	0.149	0.077	0.345
$I_f^\pi = \frac{1}{2}^+, \frac{3}{2}^+, \frac{5}{2}^+$	$s_{1/2}$	1.438	1.406	
	$d_{3/2}$	-0.181	-0.019	-0.010
	$d_{5/2}$		0.143	0.001
$K_f^\pi = \frac{1}{2}^+$	$d_{5/2}$		0.143	0.001
	$d_{7/2}$			-0.020
$\varepsilon_{\text{peak}} = 0.06 \text{ MeV}$	$g_{7/2}$			0.000
	$g_{9/2}$			-0.001
$I_f^\pi = \frac{3}{2}^+, \frac{5}{2}^+$	$d_{3/2}$	-1.074	0.199	0.046
	$d_{5/2}$		0.598	-0.026
	$g_{7/2}$			-0.023
$K_f^\pi = \frac{3}{2}^+$	$g_{7/2}$			-0.007
	$g_{9/2}$			-0.035
	$g_{9/2}$			-0.035

B. Electric dipole response in ^{37}Mg

The observed excitation energies of neighboring nuclei ^{36}Mg [57, 58] and ^{38}Mg [58] suggest that these neutron-rich magnesium isotopes lie within the island of inversion and indicate a strong quadrupole of deformation for ^{37}Mg . The parallel momentum distributions of the ^{37}Mg residues after the Coulomb breakup reactions also support the presence of strong deformation [11]. Theoretically, strong deformation is predicted in Refs. [37, 48, 59–61] within the framework of relativistic and non-relativistic mean-field theories.

The Nilsson diagram of ^{37}Mg is shown in Fig. 6, where the deformed Woods-Saxon potential is adjusted for the separation energy of last neutron to be $S_n \sim 0.2 \text{ MeV}$. As can be seen in the figure, the last neutron, with $N = 25$, may occupy the $1f_{7/2}$ orbit in the spherical limit. For the prolate deformation, the negative parity [321]1/2 orbit becomes the last occupied orbit for neutrons when $\beta_2 > 0.2$. From Table V, we can see that the deformed wave function of [321]1/2 has the components of $p_{1/2}$, $p_{3/2}$, $f_{5/2}$ and $f_{7/2}$ orbits, and indicates a large halo con-

FIG. 6. Same as Fig. 1, but for ^{37}Mg . The asymptotic quantum-numbers $[Nn_z\Lambda]\Omega$ represent the single-particle level, which is particularly important in the present subject.

tribution of p -wave with 58% probability.

Figure 7 shows the $E1$ response from a halo configuration [321]1/2 with $I_i^\pi = \frac{3}{2}^-, K_i^\pi = \frac{1}{2}^-$ to the positive parity states with $K_f^\pi = \frac{1}{2}^+$ and $K_f^\pi = \frac{3}{2}^+$. Similar to the halo configuration [330]1/2 in ^{31}Ne , the excitation to the $I_f^\pi = \frac{1}{2}^+, \frac{3}{2}^+$ and $\frac{5}{2}^+$ with $K_f^\pi = \frac{1}{2}^+$ dominates the $E1$ transition strength, while there is almost no strength for the states with $K_f^\pi = \frac{3}{2}^+$. Since the transition matrix elements for $K_f^\pi = \frac{1}{2}^+$ have the same sign for the initial $p_{3/2}$ and $p_{1/2}$ configuration in Table V, the dipole response becomes large for the $K_f^\pi = \frac{1}{2}^+$ state. On the other hand, the transition matrix elements have opposite signs for $K_f^\pi = \frac{3}{2}^+$, which induce a large cancellation for the dipole response, as shown in Fig. 7. The dip at $\omega - S = 0.7 \text{ MeV}$ is also due to the cancellation among the matrix elements of the transition to $K_f^\pi = 1/2^+$ state. The $E1$ response increases up to 2 MeV, then decreases after 5 MeV and goes to zero eventually.

The dipole response with the pure halo $2p_{3/2}$ configuration with the separation energy $S_n = 0.22 \text{ MeV}$ is shown in Fig. 8. The $E1$ strength in Fig. 8 is a factor 2 larger than the response to the deformed wave function in Fig. 7, which is caused by 58% probability of halo p -wave component of [321]1/2 orbit. The integrated $E1$ strength is listed in Table VI. Because of large contributions from

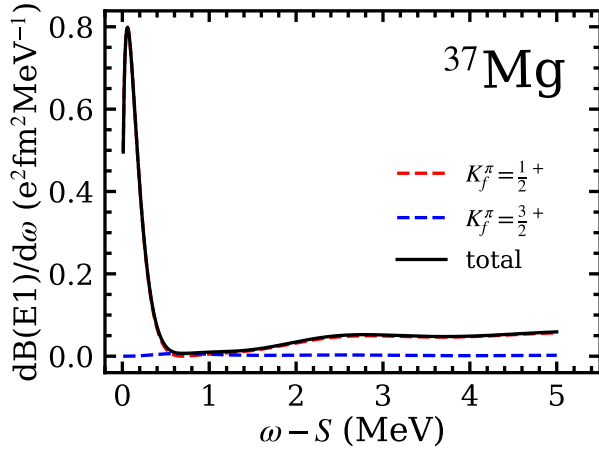


FIG. 7. (Color online) Dipole strength distribution in ^{37}Mg calculated as a function of the excitation energy (referred to the particle threshold). The wave function of the ground state takes the $[321]1/2, I_i^\pi = 3/2^-$ configuration at $\beta_2 = 0.46$, which is calculated using the deformed Woods-Saxon potential, corresponding to the single-neutron separation energy of 0.22 MeV. The $p_{1/2}$, $p_{3/2}$, $f_{5/2}$ and $f_{7/2}$ orbitals are included in the calculation of the $[321]1/2$ orbit.

s -wave and d -wave component of wave functions in the final states, the pure $2p_{3/2}$ configuration has almost factor 5 larger than the deformed configuration $[321]1/2$.

TABLE VI. Dipole transition probabilities $B(E1)$ ($e^2\text{fm}^2$) for ^{37}Mg with different initial wave functions. The initial state is taken as $I_i^\pi = \frac{3}{2}^-$ and $K_i^\pi = \frac{1}{2}^-$.

Initial state	$[321]1/2$	$2p_{3/2}$
$K_f^\pi = \frac{1}{2}^+$	0.333	0.896
$K_f^\pi = \frac{3}{2}^+$	0.013	0.601
Total	0.346	1.497

IV. SUMMARY

We studied the $E1$ response from the deformed halo orbits in ^{31}Ne and ^{37}Mg taking into account all possible configurations in the Nilsson orbits, whose separation energy is adjusted to the experimental one. There are three possible configurations of the ground state in ^{31}Ne , i.e., the Nilsson orbits, $[321]3/2$, $[330]1/2$ and $[202]3/2$ depending on the magnitude of β_2 value. We pointed out that the two halo configurations, $[321]3/2$ and $[330]1/2$, contain large amplitudes of halo p -wave components, which significantly enhance the threshold strength. On the other hand, the non-halo configuration $[202]3/2$ have some enhancement of the soft dipole strength in the integrated $E1$ value in Table IV. However, the peak does not show any sign of enhancement

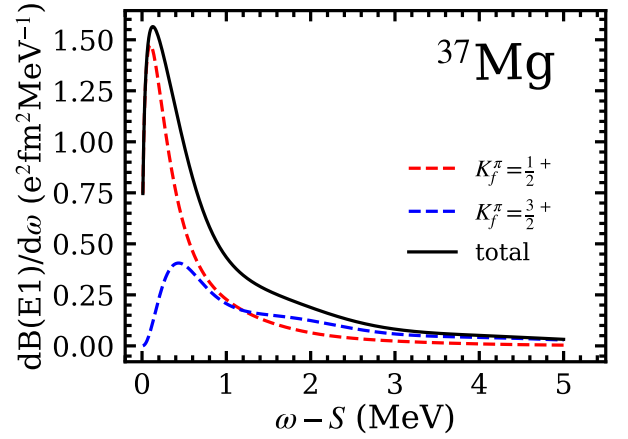


FIG. 8. (Color online) Same as Fig. 7, but for the pure $2p_{3/2}$ configuration with the separation energy $S_n = 0.22$ MeV.

because of much broader width than the halo configurations. The two halo configurations, $[321]3/2$ at $\beta_2 = 0.5$ and $[330]1/2$ at $\beta_2 = 0.24$, show a strong soft dipole peaks near the threshold with the different peak heights: that of the $[330]1/2$ configuration is nearly 2 times larger than that of the $[321]3/2$ configuration because of different halo p -wave amplitudes. This difference will help to assign the configuration, equivalently the magnitude of β_2 deformation if the empirical $E1$ strength is extracted from the Coulomb breakup cross sections, for example $^{31}\text{Ne} + ^{208}\text{Pb}$ reaction.

Another deformed halo nucleus ^{37}Mg is also studied with the same deformed Woods-Saxon model. The separation energy is constrained by recent empirical information of $S_n \sim 200$ keV at a large deformation $\beta_2 = 0.46$. The last neutron configuration is assigned as $[321]1/2$ Nilsson orbit which involves also large halo p -orbit configurations. The calculated $E1$ response shows a strong soft dipole nature. Compared with soft dipole strength of pure p -wave configuration in Fig. 8, the deformation effect quenches to some extent the peak of $E1$ strength distribution. Experimental confirmation of soft dipole strength is highly desired to assign the deformation and the configuration of the last neutron orbit in ^{37}Mg . Theoretically we will introduce more elaborate model such as deformed quasi-particle random phase approximation (QRPA) on top of deformed Hartree-Fock model with continuum coupling or time-dependent finite amplitude approximation with DRHBc in near future [62].

ACKNOWLEDGMENTS

We thank Koichi Hagino for providing us with his deformed Woods-Saxon code. Fruitful discussions with Xiang-Xiang Sun, Yu-Ting Rong, Yi-Ming Jiang and Xin-Le Shang are gratefully acknowledged. This work is supported by the National Natural Science Foundation of China (Grant Nos. 12347139, 12047503, 12375118,

12435008, and W2412043), the Chinese Academy of Sciences (CAS) President's International Fellowship Initiative (PIFI, Grant No. 2024PVA0003), the National Key R&D Program of China (Grant Nos. 2023YFA1606503 and 2024YFE0109801) and the CAS Strategic Priority

Research Program (Grant No. XDB34010000). The results described in this paper are obtained on the High-performance Computing Cluster of ITP-CAS and the Se-Grid of the Supercomputing Center, Computer Network Information Center of Chinese Academy of Sciences.

-
- [1] I. Tanihata, H. Savajols, and R. Kanungo, *Prog. Part. Nucl. Phys.* **68**, 215 (2013).
- [2] S.-G. Zhou, *PoS INPC2016*, 373 (2017), arXiv:1703.09045 [nucl-th].
- [3] Y. Ye, X. Yang, H. Sakurai, and B. Hu, *Nat. Rev. Phys.* **7**, 21 (2025).
- [4] I. Tanihata, H. Hamagaki, O. Hashimoto, Y. Shida, N. Yoshikawa, K. Sugimoto, O. Yamakawa, T. Kobayashi, and N. Takahashi, *Phys. Rev. Lett.* **55**, 2676 (1985).
- [5] I. Tanihata, T. Kobayashi, O. Yamakawa, S. Shimoura, K. Ekuni, K. Sugimoto, N. Takahashi, T. Shimoda, and H. Sato, *Phys. Lett. B* **206**, 592 (1988).
- [6] M. Fukuda, T. Ichihara, N. Inabe, T. Kubo, H. Kumagai, T. Nakagawa, Y. Yano, I. Tanihata, M. Adachi, K. Asahi, M. Kouguchi, M. Ishihara, H. Sagawa, and S. Shimoura, *Phys. Lett. B* **268**, 339 (1991).
- [7] D. Bazin, B. Brown, J. Brown, M. Fauerbach, M. Hellström, S. Hirzebruch, J. Kelley, R. Kryger, D. Morrissey, R. Pfaff, C. Powell, B. Sherrill, and M. Thoennessen, *Phys. Rev. Lett.* **74**, 3569 (1995).
- [8] T. Nakamura, N. Fukuda, T. Kobayashi, N. Aoi, H. Iwasaki, T. Kubo, A. Mengoni, M. Notani, H. Otsu, H. Sakurai, S. Shimoura, T. Teranishi, Y. X. Watanabe, K. Yoneda, and M. Ishihara, *Phys. Rev. Lett.* **83**, 1112 (1999).
- [9] T. Nakamura, N. Kobayashi, Y. Kondo, Y. Satou, N. Aoi, H. Baba, S. Deguchi, N. Fukuda, J. Gibelin, N. Inabe, M. Ishihara, D. Kameda, Y. Kawada, T. Kubo, K. Kusaka, A. Mengoni, T. Motobayashi, T. Ohnishi, M. Ohtake, N. A. Orr, H. Otsu, T. Otsuka, A. Saito, H. Sakurai, S. Shimoura, T. Sumikama, H. Takeda, E. Takeshita, M. Takechi, S. Takeuchi, K. Tanaka, K. N. Tanaka, N. Tanaka, Y. Togano, Y. Utsuno, K. Yoneda, A. Yoshida, and K. Yoshida, *Phys. Rev. Lett.* **103**, 262501 (2009).
- [10] T. Nakamura, N. Kobayashi, Y. Kondo, Y. Satou, J. A. Tostevin, Y. Utsuno, N. Aoi, H. Baba, N. Fukuda, J. Gibelin, N. Inabe, M. Ishihara, D. Kameda, T. Kubo, T. Motobayashi, T. Ohnishi, N. A. Orr, H. Otsu, T. Otsuka, H. Sakurai, T. Sumikama, H. Takeda, E. Takeshita, M. Takechi, S. Takeuchi, Y. Togano, and K. Yoneda, *Phys. Rev. Lett.* **112**, 142501 (2014).
- [11] N. Kobayashi, T. Nakamura, Y. Kondo, J. A. Tostevin, Y. Utsuno, N. Aoi, H. Baba, R. Barthelemy, M. A. Famiano, N. Fukuda, N. Inabe, M. Ishihara, R. Kanungo, S. Kim, T. Kubo, G. S. Lee, H. S. Lee, M. Matsushita, T. Motobayashi, T. Ohnishi, N. A. Orr, H. Otsu, T. Otsuka, T. Sako, H. Sakurai, Y. Satou, T. Sumikama, H. Takeda, S. Takeuchi, R. Tanaka, Y. Togano, and K. Yoneda, *Phys. Rev. Lett.* **112**, 242501 (2014).
- [12] M. Takechi, S. Suzuki, D. Nishimura, M. Fukuda, T. Ohtsubo, M. Nagashima, T. Suzuki, T. Yamaguchi, A. Ozawa, T. Moriguchi, H. Ohishi, T. Sumikama, H. Geissel, N. Aoi, R.-J. Chen, D.-Q. Fang, N. Fukuda, S. Fukuoka, H. Furuki, N. Inabe, Y. Ishibashi, T. Itoh, T. Izumikawa, D. Kameda, T. Kubo, M. Lantz, C. S. Lee, Y.-G. Ma, K. Matsuta, M. Mihara, S. Momota, D. Nagae, R. Nishikiori, T. Niwa, T. Ohnishi, K. Okumura, M. Ohtake, T. Ogura, H. Sakurai, K. Sato, Y. Shimbara, H. Suzuki, H. Takeda, S. Takeuchi, K. Tanaka, M. Tanaka, H. Uenishi, M. Winkler, Y. Yanagisawa, S. Watanabe, K. Minomo, S. Tagami, M. Shimada, M. Kimura, T. Matsumoto, Y. R. Shimizu, and M. Yahiyo, *Phys. Rev. C* **90**, 061305 (2014).
- [13] T. Suzuki, Y. Ogawa, M. Chiba, M. Fukuda, N. Iwasa, T. Izumikawa, R. Kanungo, Y. Kawamura, A. Ozawa, T. Suda, I. Tanihata, S. Watanabe, T. Yamaguchi, and Y. Yamaguchi, *Phys. Rev. Lett.* **89**, 012501 (2002).
- [14] Z. H. Yang, Y. Kubota, A. Corsi, K. Yoshida, X.-X. Sun, J. G. Li, M. Kimura, N. Michel, K. Ogata, C. X. Yuan, Q. Yuan, G. Authelet, H. Baba, C. Caesar, D. Calvet, A. Delbart, M. Dozono, J. Feng, F. Flavigny, J.-M. Gheller, J. Gibelin, A. Giganon, A. Gillibert, K. Hasegawa, T. Isobe, Y. Kanaya, S. Kawakami, D. Kim, Y. Kiyokawa, M. Kobayashi, N. Kobayashi, T. Kobayashi, Y. Kondo, Z. Korkulu, S. Koyama, V. Lapoux, Y. Maeda, F. M. Marqués, T. Motobayashi, T. Miyazaki, T. Nakamura, N. Nakatsuka, Y. Nishio, A. Obertelli, A. Ohkura, N. A. Orr, S. Ota, H. Otsu, T. Ozaki, V. Panin, S. Paschalis, E. C. Pollacco, S. Reichert, J.-Y. Roussé, A. T. Saito, S. Sakaguchi, M. Sako, C. Santamaria, M. Sasano, H. Sato, M. Shikata, Y. Shimizu, Y. Shindo, L. Stuhl, T. Sumikama, Y. L. Sun, M. Tabata, Y. Togano, J. Tsubota, F. R. Xu, J. Yasuda, K. Yoneda, J. Zenihiro, S.-G. Zhou, W. Zuo, and T. Uesaka, *Phys. Rev. Lett.* **126**, 082501 (2021).
- [15] K. J. Cook, T. Nakamura, Y. Kondo, K. Hagino, K. Ogata, A. T. Saito, N. L. Achouri, T. Aumann, H. Baba, F. Delaunay, Q. Deshayes, P. Doornenbal, N. Fukuda, J. Gibelin, J. W. Hwang, N. Inabe, T. Isobe, D. Kameda, D. Kanno, S. Kim, N. Kobayashi, T. Kobayashi, T. Kubo, S. Leblond, J. Lee, F. M. Marqués, R. Minakata, T. Motobayashi, K. Muto, T. Murakami, D. Murai, T. Nakashima, N. Nakatsuka, A. Navin, S. Nishi, S. Ogoshi, N. A. Orr, H. Otsu, H. Sato, Y. Satou, Y. Shimizu, H. Suzuki, K. Takahashi, H. Takeda, S. Takeuchi, R. Tanaka, Y. Togano, J. Tsubota, A. G. Tuff, M. Vandebrouck, and K. Yoneda, *Phys. Rev. Lett.* **124**, 212503 (2020).
- [16] K. Tanaka, T. Yamaguchi, T. Suzuki, T. Ohtsubo, M. Fukuda, D. Nishimura, M. Takechi, K. Ogata, A. Ozawa, T. Izumikawa, T. Aiba, N. Aoi, H. Baba, Y. Hashizume, K. Inafuku, N. Iwasa, K. Kobayashi, M. Komuro, Y. Kondo, T. Kubo, M. Kurokawa, T. Matsuyama, S. Michimasa, T. Motobayashi, T. Nakabayashi, S. Nakajima, T. Nakamura, H. Sakurai, R. Shinoda, M. Shinohara, H. Suzuki, E. Takeshita, S. Takeuchi,

- Y. Togano, K. Yamada, T. Yasuno, and M. Yoshitake, *Phys. Rev. Lett.* **104**, 062701 (2010).
- [17] S. Bagchi, R. Kanungo, Y. K. Tanaka, H. Geissel, P. Doornenbal, W. Horiuchi, G. Hagen, T. Suzuki, N. Tsunoda, D. S. Ahn, H. Baba, K. Behr, F. Browne, S. Chen, M. L. Cortés, A. Estradé, N. Fukuda, M. Holl, K. Itahashi, N. Iwasa, G. R. Jansen, W. G. Jiang, S. Kaur, A. O. Macchiavelli, S. Y. Matsumoto, S. Momiyama, I. Murray, T. Nakamura, S. J. Novario, H. J. Ong, T. Otsuka, T. Papenbrock, S. Paschalis, A. Prochazka, C. Scheidenberger, P. Schrock, Y. Shimizu, D. Steppenbeck, H. Sakurai, D. Suzuki, H. Suzuki, M. Takechi, H. Takeda, S. Takeuchi, R. Taniuchi, K. Wimmer, and K. Yoshida, *Phys. Rev. Lett.* **124**, 222504 (2020).
- [18] H. Sagawa, *Phys. Lett. B* **286**, 7 (1992).
- [19] K. Riisager, A. Jensen, and P. Møller, *Nucl. Phys. A* **548**, 393 (1992).
- [20] J. Meng and P. Ring, *Phys. Rev. Lett.* **77**, 3963 (1996).
- [21] J. Meng, H. Toki, S. Zhou, S. Zhang, W. Long, and L. Geng, *Prog. Part. Nucl. Phys.* **57**, 470 (2006).
- [22] J. Meng and S. G. Zhou, *J. Phys. G: Nucl. Part. Phys.* **42**, 093101 (2015).
- [23] A. Bohr and B. R. Mottelson, *Nuclear Structure Vol. II* (1975).
- [24] I. Hamamoto, *Phys. Rev. C* **72**, 024301 (2005).
- [25] T. Nakamura, T. Motobayashi, Y. Ando, A. Mengoni, T. Nishio, H. Sakurai, S. Shimoura, T. Teranishi, Y. Yanagisawa, and M. Ishihara, *Phys. Lett. B* **394**, 11 (1997).
- [26] T. Nakamura, A. M. Vinodkumar, T. Sugimoto, N. Aoi, H. Baba, D. Bazin, N. Fukuda, T. Gomi, H. Hasegawa, N. Imai, M. Ishihara, T. Kobayashi, Y. Kondo, T. Kubo, M. Miura, T. Motobayashi, H. Otsu, A. Saito, H. Sakurai, S. Shimoura, K. Watanabe, Y. X. Watanabe, T. Yakushiji, Y. Yanagisawa, and K. Yoneda, *Phys. Rev. Lett.* **96**, 252502 (2006).
- [27] T. Misu, W. Nazarewicz, and S. Åberg, *Nucl. Phys. A* **614**, 44 (1997).
- [28] I. Hamamoto, *Phys. Rev. C* **85**, 064329 (2012).
- [29] I. Hamamoto, *Phys. Rev. C* **81**, 021304 (2010).
- [30] Y. Urata, K. Hagino, and H. Sagawa, *Phys. Rev. C* **83**, 041303 (2011).
- [31] Y. Urata, K. Hagino, and H. Sagawa, *Phys. Rev. C* **86**, 044613 (2012).
- [32] Y. Urata, K. Hagino, and H. Sagawa, *Phys. Rev. C* **96**, 064311 (2017).
- [33] T. Otsuka, N. Fukunishi, and H. Sagawa, *Phys. Rev. Lett.* **70**, 1385 (1993).
- [34] T. T. S. Kuo, F. Krmpotić, and Y. Tzeng, *Phys. Rev. Lett.* **78**, 2708 (1997).
- [35] P. Descouvemont, *Nucl. Phys. A* **655**, 440 (1999).
- [36] S.-G. Zhou, J. Meng, P. Ring, and E.-G. Zhao, *Phys. Rev. C* **82**, 011301 (2010).
- [37] L. Li, J. Meng, P. Ring, E.-G. Zhao, and S.-G. Zhou, *Phys. Rev. C* **85**, 024312 (2012).
- [38] Y. N. Zhang, J. C. Pei, and F. R. Xu, *Phys. Rev. C* **88**, 054305 (2013).
- [39] J. C. Pei, Y. N. Zhang, and F. R. Xu, *Phys. Rev. C* **87**, 051302 (2013).
- [40] X.-X. Sun, J. Zhao, and S.-G. Zhou, *Phys. Lett. B* **785**, 530 (2018).
- [41] H. Nakada and K. Takayama, *Phys. Rev. C* **98**, 011301 (2018).
- [42] K. Y. Zhang, D. Y. Wang, and S. Q. Zhang, *Phys. Rev. C* **100**, 034312 (2019).
- [43] X.-X. Sun, J. Zhao, and S.-G. Zhou, *Nucl. Phys. A* **1003**, 122011 (2020).
- [44] X.-X. Sun, *Phys. Rev. C* **103**, 054315 (2021).
- [45] X.-X. Sun and S.-G. Zhou, *Sci. Bull.* **66**, 2072 (2021).
- [46] Q. Chai, H. Chen, M. Zha, J. Pei, and F. Xu, *Symmetry* **14**, 10.3390/sym14020215 (2022).
- [47] K. Y. Zhang, P. Papakonstantinou, M.-H. Mun, Y. Kim, H. Yan, and X.-X. Sun, *Phys. Rev. C* **107**, L041303 (2023).
- [48] K. Zhang, S. Yang, J. An, S. Zhang, P. Papakonstantinou, M.-H. Mun, Y. Kim, and H. Yan, *Phys. Lett. B* **844**, 138112 (2023).
- [49] J.-L. An, K.-Y. Zhang, Q. Lu, S.-Y. Zhong, and S.-S. Zhang, *Phys. Lett. B* **849**, 138422 (2024).
- [50] R. Takatsu, Y. Suzuki, W. Horiuchi, and M. Kimura, *Phys. Rev. C* **107**, 024314 (2023).
- [51] I. Hamamoto, *Phys. Rev. C* **100**, 014324 (2019).
- [52] Y. Yanagisawa, M. Notani, H. Sakurai, M. Kunibu, H. Akiyoshi, N. Aoi, H. Baba, K. Demichi, N. Fukuda, H. Hasegawa, Y. Higurashi, M. Ishihara, N. Iwasa, H. Iwasaki, T. Gomi, S. Kanno, M. Kurokawa, Y. Matsuyama, S. Michimasa, T. Minemura, T. Mizoi, T. Nakamura, A. Saito, M. Serata, S. Shimoura, T. Sugimoto, E. Takeshita, S. Takeuchi, K. Ue, K. Yamada, K. Yoneda, and T. Motobayashi, *Phys. Lett. B* **566**, 84 (2003).
- [53] P. Doornenbal, H. Scheit, N. Aoi, S. Takeuchi, K. Li, E. Takeshita, H. Wang, H. Baba, S. Deguchi, N. Fukuda, H. Geissel, R. Gernhäuser, J. Gibelin, I. Hachiuma, Y. Hara, C. Hinke, N. Inabe, K. Itahashi, S. Itoh, D. Kameda, S. Kanno, Y. Kawada, N. Kobayashi, Y. Kondo, R. Krücken, T. Kubo, T. Kuboki, K. Kusaka, M. Lantz, S. Michimasa, T. Motobayashi, T. Nakamura, T. Nakao, K. Namiyama, S. Nishimura, T. Ohnishi, M. Ohtake, N. A. Orr, H. Otsu, K. Ozeki, Y. Satou, S. Shimoura, T. Sumikama, M. Takechi, H. Takeda, K. N. Tanaka, K. Tanaka, Y. Togano, M. Winkler, Y. Yanagisawa, K. Yoneda, A. Yoshida, K. Yoshida, and H. Sakurai, *Phys. Rev. Lett.* **103**, 032501 (2009).
- [54] D. T. Yordanov, M. Kowalska, K. Blaum, M. De Rydt, K. T. Flanagan, P. Lievens, R. Neugart, G. Neyens, and H. H. Stroke, *Phys. Rev. Lett.* **99**, 212501 (2007).
- [55] S.-G. Zhou, J. Meng, and P. Ring, *Phys. Rev. C* **68**, 034323 (2003).
- [56] A. Poves and J. Retamosa, *Nucl. Phys. A* **571**, 221 (1994).
- [57] P. Doornenbal, H. Scheit, S. Takeuchi, N. Aoi, K. Li, M. Matsushita, D. Steppenbeck, H. Wang, H. Baba, E. Ideguchi, N. Kobayashi, Y. Kondo, J. Lee, S. Michimasa, T. Motobayashi, A. Poves, H. Sakurai, M. Takechi, Y. Togano, and K. Yoneda, *Phys. Rev. C* **93**, 044306 (2016).
- [58] P. Doornenbal, H. Scheit, S. Takeuchi, N. Aoi, K. Li, M. Matsushita, D. Steppenbeck, H. Wang, H. Baba, H. Crawford, C. R. Hoffman, R. Hughes, E. Ideguchi, N. Kobayashi, Y. Kondo, J. Lee, S. Michimasa, T. Motobayashi, H. Sakurai, M. Takechi, Y. Togano, R. Winkler, and K. Yoneda, *Phys. Rev. Lett.* **111**, 212502 (2013).
- [59] Z. Ren, Z. Zhu, Y. Cai, and G. Xu, *Phys. Lett. B* **380**, 241 (1996).
- [60] C. Jin-Gen, C. Xiang-Zhou, W. Ting-Tai, M. Yu-Gang, R. Zhong-Zhou, F. De-Qing, Z. Chen, W. Yi-Bin, G. Wei, Z. Xing-Fei, W. Kun, M. Guo-Liang, T. Wen-Dong,

- C. Jin-Hui, Y. Ting-Zhi, Z. Jia-Xu, M. Chun-Wang, and S. Wen-Qing, Chin. Phys. **14**, 2444 (2005).
- [61] X.-Y. Xiong, J.-C. Pei, Y.-N. Zhang, and Y. Zhu, Chin. Phys. C **40**, 024101 (2016).
- [62] X. Sun and J. Meng, Phys. Rev. C **105**, 044312 (2022).